JOURNAL OF SYNCHROTRON RADIATION

ISSN 1600-5775

C, N dual-doped ZnO nanofoams: a potential antimicrobial agent, an efficient visible light photocatalyst and SXAS studies

A. B. V. Kiran Kumar,[a,b]* Sanjeev Billa,[a] Edugulla Girija Shankar[a] and M. C. S. Subha[c]

[a]Amity Institute of Nanotechnology, Amity University, Sector 125, Noida, Uttar Pradesh 201301, India, [b]Vijaya Lab, Buchireddypalem, Nellore District, Andhra Pradesh 524305, India, and [c]Department of Chemistry, Sri Krishnadevaraya University, Anantapur, Andhra Pradesh 515003, India. *Correspondence e-mail: bharanichem@gmail.com

Received 2 April 2019
Accepted 5 October 2019

Edited by I. Lindau, SLAC/Stanford University, USA

Keywords: CNZ nanofoams; soft template; soft X-ray absorption spectroscopy (SXAS); photocatalytic activity; antimicrobial activity; doping.

Supporting information: this article has supporting information at journals.iucr.org/s

It is crucial to develop an environmentally friendly and low-cost method to treat industrial effluent that contains soluble dyes and microbes. Most of the photocatalysts have been studied using an external light source that increases the cost of the purification process of effluent. This study focuses on developing efficient solar photocatalytic nanofoams. The controlled growth of ZnO nanofoams (CNZ nanofoams) in a simple method of thermal oxidation using a soft template is reported. Prepared nanofoams are characterized using X-ray diffraction, scanning electon microscopy and synchrotron soft X-ray absorption spectroscopy. By photocatalysis studies under direct sunlight it was found that within 120 min CNZ nanofoams degraded 99% of the dye. In addition, antimicrobial studies of multi-drug-resistant *E. Fergusonii* isolated from waste-water was carried out. These antimicrobial results showed a good inhibition zone, indicating that prepared nanofoams are both an effective solar photocatalyst and an antimicrobial agent.

1. Introduction

In the contemporary world, the textile and pharmaceutical industries are the two major manufacturing sectors, and play a key role in the economic growth of many countries. However, the industrial effluents involved in these industries contain organic pollutants like dyes and toxic chemicals. Water pollution caused by these pollutants leads to serious environmental and health hazards. It is a major challenge to remove these textile effluents and toxic chemicals because of their stability and good solubility in water. Various methods such as adsorption and flocculation are extensively used for the treatment of textile effluents. Other important methods are available like pervaporation for separating organic solvents from water solutions (Dharupaneedi *et al.*, 2014; Reddy *et al.*, 2007; Adoor *et al.*, 2014; Krishna Rao *et al.*, 2006; Magalad *et al.*, 2010). However, this method is not suitable for the removal of organic soluble dyes. Nevertheless, these methods can only transfer the chemicals to the adsorbent surfaces, which leads to a secondary pollution. In view of its functionality, photocatalysis has attracted the attention of researchers to remove organic pollutants from industrial effluents. This is due to the fact that it is an environmentally friendly method and can degrade the dyes and toxic soluble chemicals completely without leaving any fragments that may cause secondary pollution (Zhang *et al.*, 2015; Kumar *et al.*, 2018).

Semiconducting metal oxide nanostructures are an important class of materials and can be used as catalysts in the

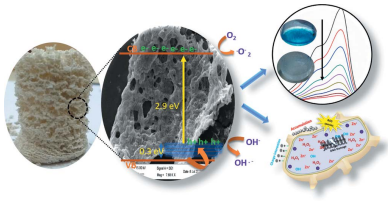

photodegradation process. Many transition metal oxide nanostructures such as TiO_2, ZnO, Fe_2O_3 and SnO_2 have been studied for the photocatalysis (Gupta *et al.*, 2015; Rani *et al.*, 2018; Liu *et al.*, 2016; Show *et al.*, 2016; Kumar & Rao, 2017). Among these metal oxide nanostructures, TiO_2 is the most studied metal oxide as a photocatalyst. Alternatively, ZnO was found to be a replacement for TiO_2 because of its similarities in stability, non-toxicity, comparatively low cost and easy processing. However, ZnO has a limitation to its use as a visible-light photocatalyst due to its wide band gap (3.3 eV) and large excitation binding energy (60 meV) (Dvorak *et al.*, 2013). To overcome this limitation, doping with non-metals such as carbon (Haibo *et al.*, 2013; Zhang *et al.*, 2015), nitrogen (Macías-Sánchez *et al.*, 2015), selenium (Dutta *et al.*, 2014), sulfur (Cho *et al.*, 2012; Khan *et al.*, 2017) *etc*. has proven to be an effective way to convert ZnO to be a visible-light photocatalyst (Yu *et al.*, 2016; da Silva *et al.*, 2017; Pascariu *et al.*, 2018).

In addition, the morphology of the photocatalyst is one of the most important factors to improve the catalytic efficiency. In general, the surface area and active sites present in the unit area will increase with a decrease in particle size, which leads to increased or higher efficiency. Based on this factor, different morphologies of ZnO such as nanorods (Ruqia *et al.*, 2017), nanosheets (Khoa *et al.*, 2014), nanowires (Baxter & Schmuttenmaer, 2006), nanotubes (Wang & Cui, 2009), nanospheres (Zhang *et al.*, 2009), nanostars (Cho *et al.*, 2012), microspheres (Wang *et al.*, 2018) *etc*. have been reported by different research groups using various preparation methods. Khoa *et al.* (2014) developed ZnO nanosheets using a hydrothermal method for photocatalytic activity. Huang *et al.* (2015) developed hierarchical ZnO nanoflowers using vapour deposition. Rao *et al.* (2012) reported the preparation of hollow and mesoporous ZnO microspheres using reflux under sonication for sensing applications. Recently, Ruqia *et al.* (2017) synthesized ZnO nanorods by the solvothermal method and studied their optical properties. More recently, we reported brain sponge CNClZnO nanostructures for solar light photocatalysis (Ghosh *et al.*, 2018).

Further, literature studies suggest that ZnO nanoparticles (Qi *et al.*, 2017) exhibit antimicrobial property and are proven as potential antimicrobial agents for *Staphylococcus aureus* (Kadiyala *et al.*, 2018) and *Escherichia coli* (Hameed *et al.*, 2016). ZnO nanoparticles have been used for various biomedical applications due to their large surface area and the ability to generate reactive oxygen species in the presence of light, which causes potential damage to microbial cells, while other reports suggest that ZnO nanoparticles are potential growth inhibitors of fungi (Das *et al.*, 2017). This is why ZnO nanoparticles are used to treat microbial polluted wastewater. For instance, Fiorentino *et al.* (2015) found that ZnO nanoparticles are able to resist *E. coli* which is mainly found in urban wastewater. However, very few research studies have been performed on ZnO resistance to multi-drug-resistant (MDR) strains (Das *et al.*, 2017). Therefore, studying the doped ZnO antimicrobial activity against MDR bacteria is an emerging research area. In this report, we present our studies on the antimicrobial effect of prepared CNZ nanofoams against MDR *E. Fergusonii*, isolated from the wastewater collected from urban areas.

2. Experimental

2.1. Materials and methods

Polyvinyl pyrrolidone (K30), zinc nitrate hexahydrate [$Zn(NO_3)_2{\cdot}6H_2O$], absolute ethanol and methylene blue, NaCl and Agar powder were purchased from Merck. Beef extract and peptone were purchased from Sigma-Aldrich. All these reagents were used as received. Distilled water, which was used to carry out the whole experiment, was collected from the department. An alumina crucible was used for calcination at the three temperatures 300°C, 400°C and 500°C.

2.2. Synthesis of carbon and nitrogen ZnO nanofoams

Carbon and nitrogen dual-doped ZnO nanofoams were prepared using the two-step process according to Kiran Kumar & Sanjeev (2018). In the first step, an appropriate amount of K30 was dissolved in 50 ml of water and alcohol mixture using a magnetic stirrer; zinc nitrate hexahydrate was added to the solution and stirring was continued until a clear solution was formed. The resulting polymer and zinc nitrate mixture was heated to form K30–Zn blend. In the second step, the blend was transferred into an alumina crucible and annealed in a muffle furnace at various temperatures (*i.e.* 300°C, 400°C, 500°C) to obtain ZnO nanofoams. The prepared ZnO nanofoams were named as CNZ300, CNZ400 and CNZ500.

2.3. Characterization

Morphological studies were performed using a ZEISS scanning electron microscope (SEM) with an accelerating voltage of 10 kV with Au coating. Powder X-ray diffraction (XRD) studies were performed on Bruker Cu $K\alpha$ (1.5405 Å) at a scan rate of 3° min^{-1} at 40 kV from 20° to 80° 2θ. X-ray absorption spectroscopy (XAS) studies performed for all CNZ nanofoams were in total electron yield (TEY) mode at beamline 01, Indus 2, RRCAT, India. UV–VIS diffusive reflectance spectroscopy was performed using a UV-2600 model Shimadzu UV–Vis–NIR spectrophotometer from 200 nm to 800 nm.

2.4. Photocatalytic activity

Photocatalytic studies were performed under sunlight irradiation. This experiment was carried out using methylene blue (10 p.p.m.), in the presence of a CNZ photocatalyst (0.1 g). The initial sample of 3 ml was collected before placing it under sunlight and the rest of the samples were collected at an interval of 15 min for 2 h. Finally, the collected samples were analysed using the UV–Vis spectrophotometer from 200 nm to 800 nm.

2.5. Antimicrobial activity

The antimicrobial activity of CNZ nanofoams was studied against MDR *E. Fergusonii* (Pasupuleti *et al.*, 2017). The agar well diffusion method was used to study the antimicrobial property of the CNZ nanofoams. Initially, 200 ml of nutrient agar media was prepared using 1 g of NaCl and peptone each, 3 g of agar powder and 0.6 g of beef extract. Then, this media was sterilized by autoclaving and was later utilized to prepare nutrient agar plates by their solidification on sterilized Petri plates. Using a spreader, 5 µl of the aforementioned bacterial strain was spread uniformly over the solidified media on the Petri plates. After spreading the strain, a well borer was used to create the required number of wells in the agar plates. Different concentrations of CNZ300, CNZ400 and CNZ500, namely 1% and 5% each, were taken. 25 µl of CNZ300, CNZ400 and CNZ500 were loaded in different concentrations into their respective wells in the agar plates and these plates were sealed with parafilm to secure them from undesired contaminations. Then, the loaded Petri plates were incubated for 24 h at 37°C. The samples diffuse into the agar and restrict bacterial growth, creating a distinct zone around the wells called the zone of inhibition. The diameters of these inhibition zones were measured.

3. Results and discussion

The higher photocatalytic efficiency of ZnO can be achieved by altering the band gap and controlling the morphology. Nanofoams are efficient nanostructures, widely used for photocatalysis due to their unique properties such as low density, high porosity and large surface area. Such unique properties will increase the adsorption rate of the organic pollutants and fasten the catalytic activity under direct sunlight. To the best of our knowledge, no studies have been reported on carbon and nitrogen ZnO nanofoams and their application on photocatalysis. Therefore, the present investigation aimed at developing ZnO nanofoams to study the dopant effect on structural and catalytic properties of ZnO. A simple and effective green synthetic method was proposed to synthesize these CNZ nanofoams using polymer as a foaming agent and the dopant source as well. This synthetic approach is presented as a schematic in Fig. 1. K30 and zinc nitrate hexahydrate are used as the precursors used for the synthesis of CNZ nanofoams. K30 is highly soluble in aqueous solution and alcohol and also acts as a good template for the formation of porous ZnO nanostructures due to its chemical stability and high degradation temperature.

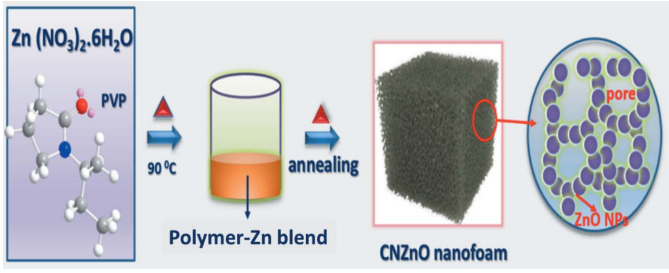

Figure 1
Schematic representation of the formation of CNZ nanofoams.

As per the schematic representation, the first step involved is to heat the two precursors in a solvent, which leads to the formation of a polymer–Zn blend due to ligand and metal ion interactions. In the second step, calcination experiments have been conducted at three different temperatures: 300°C, 400°C and 500°C. The effect of a soft template on the morphology as well as the doping nature of ZnO has been investigated by various X-ray studies such as XRD and XAS.

3.1. Morphological studies

Fig. 2 shows optical and SEM images of the CNZ nanofoams. Both types of images revealed the formation of nanofoams. In this experiment, K30 played an important role in being a foaming agent as well as a doping source for ZnO. According to thermogravimetry and differential scanning calorimetry studies (Du *et al.*, 2006), polymer degrades in the temperature range 190–300°C due to intramolecular degradation that occurs between metal ions and polymer. It can be clearly observed from Fig. 2 that the CNZ nanofoams are formed by decomposition of K30–Zn blend at 300°C, 400°C and 500°C. The process of foam formation and doping occurs simultaneously during calcination. SEM images at different magnifications are presented in Fig. 2 and Fig. S1 of the supporting information. These SEM images revealed that the pore sizes vary from the nanometre to micrometre level and a high percentage of porosity is observed in Fig. 2. It is also clear from the obtained high-magnification SEM image [Fig. 2(*e*)] that the ZnO nanoparticles are spherical in shape and are fused together to form networks in the foam. During the calcination process, the grain boundaries of the ZnO nanoparticles are diffused into each other to form connections amongst the ZnO nanoparticles.

3.2. Crystallographic studies

XRD studies were performed to investigate the effect of doping in the crystal lattice of prepared CNZ nanofoams. Fig. 3(*a*) shows the XRD patterns of CNZ300, CNZ400 and CNZ500. It is clear from Fig. 3 that no change in peak intensity has been observed for CNZ300 and CNZ400 which are calcinated at 300°C and 400°C, respectively, whereas the increased peak intensity of the CNZ500 nanofoams indicates more crystallinity. All XRD patterns of prepared CNZ nanofoams confirm the formation of hexagonal wurtzite ZnO nanostructures without any extra patterns. This indicates that the doping process did not alter the single-phase hexagonal crystal structure of the ZnO. In this context, a slight change in the XRD peak position and width indicate lattice distortions, which may be caused by the presence of defects and dopants. The compressive or tensile stress caused by the distortion leads to an XRD peak position shift towards lower or higher 2θ values. Since the ionic radii of carbon and nitrogen are greater than that of O^{2-}, this leads to tensile stress along with expansion of crystal grain size (Game *et al.*, 2012). The peak

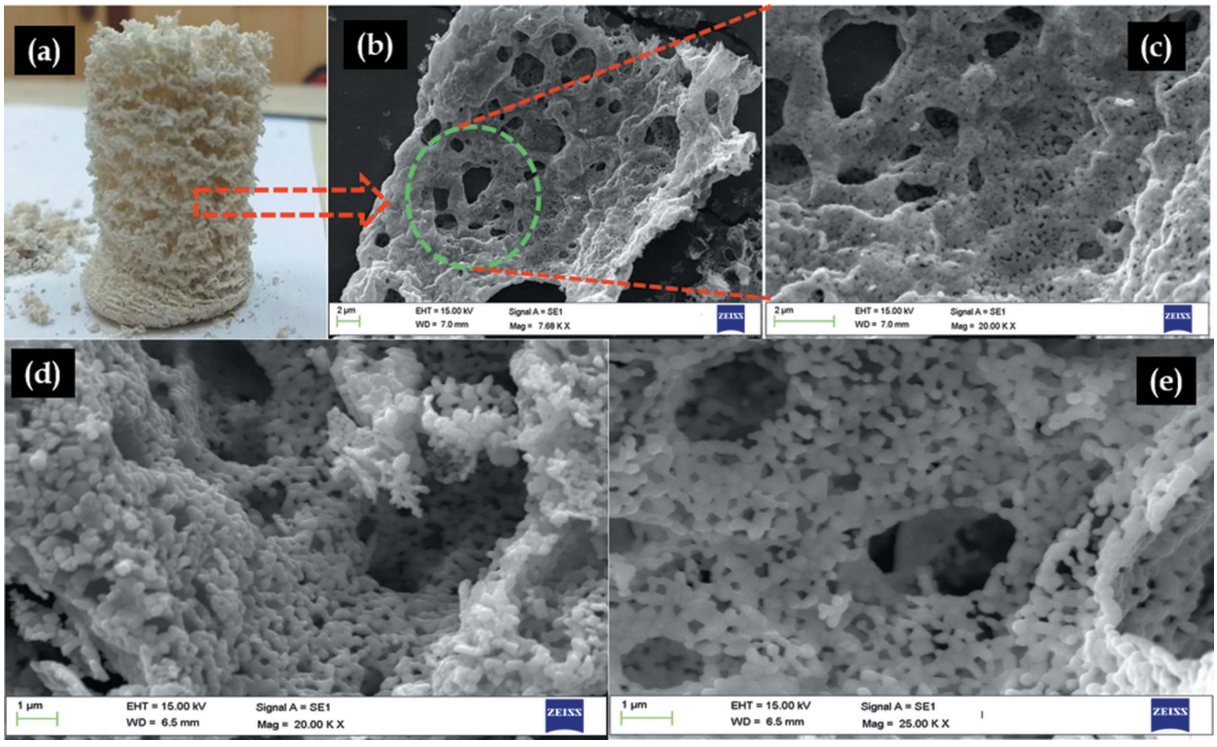

Figure 2
(*a*) Optical image of CNZ nanofoams. (*b*)–(*e*) SEM images of CNZ nanofoams.

Table 1
XRD calculations of CNZ300, CNZ400, CNZ500 and ZnO.

Sample	*a* (Å)	*c* (Å)	*d* (Å)	*D* (nm)	*β* (°)	*ε*	*V* (Å^3)
300	3.257	5.210	0.251	43.02	0.213	0.163	47.875
400	3.262	5.218	0.252	44.65	0.199	0.152	48.091
500	3.262	5.219	0.252	52.84	0.171	0.131	48.093
ZnO	3.251	5.203	0.251	40.02	0.135	0.103	47.632

shift towards higher angle and the reduction in the peak sharpness of significant (101) patterns of CNZ nanofoams are the two main observations from Fig. 3(*b*). This indicates tensile stress in the crystal lattice, which is further evidence of doping of carbon and nitrogen in the oxygen lattice. In CNZ nanofoams, both Zn and O atoms tetrahedrally coordinate to each other, and are present in equivalent positions according to Bragg's law (Bindu & Thomas, 2014). The values of lattice parameters *a* and *c*, crystallite size *D* and volume *V* (Basyooni *et al.*, 2017) are calculated using the following formulae and are listed in Table 1. The crystallite size (*D*) is calculated for ZnO and all three CNZ nanofoams using Scherer's formula (Alexander & Klug, 1950):

$$\text{Bragg law:} \quad n\lambda = 2d\sin\theta. \tag{1}$$

$$\text{Crystallite size:} \quad D = \frac{K\lambda}{\beta_{hkl}\cos\theta}. \tag{2}$$

$$\text{Volume of the unit cell:} \quad V = \frac{\sqrt{3}}{2}a^2c. \tag{3}$$

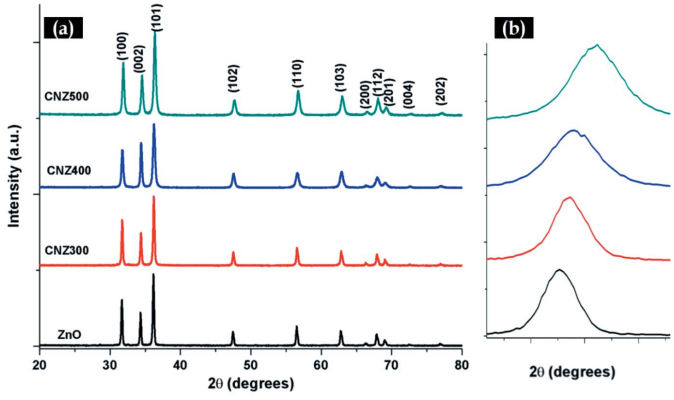

Figure 3
(*a*) XRD patterns of CNZ300, CNZ400, CNZ500 and ZnO. (*b*) Magnified (101) peak shift towards higher 2*θ*.

$$\text{Strain-induced broadening in powders:} \quad \varepsilon = \frac{\beta_{hkl}}{4\tan\theta}. \tag{4}$$

The average crystallite size calculated for the (100), (002) and (101) peaks using the the full width at half-maximum (FWHM) has increased from 43.02 to 52.84 for CNZ nanofoams when compared with ZnO (40.02). It is ascribed to be the grain boundaries increase with increase in the calcination temperatures. Simultaneously, the volume and lattice parameters of CNZ nanofoams also increased with the increase in calcination temperature from 300°C to 500°C as listed in Table 1. While calcination is carried out at higher temperatures, defects and vacancies at grain boundaries tend to reduce

due to coalescence. It can be concluded that the single-phase crystal structure confirms the substitution of carbon and nitrogen into the lattice sites of oxygen. Further XAS studies have been carried out to confirm carbon and nitrogen as dopants in the crystal lattice.

3.3. X-ray absorption spectroscopy studies

Fig. 4 shows the X-ray absorption spectroscopy of the O *K*-edge, N *K*-edge, C *K*-edge and Zn *L*-edge which confirms carbon and nitrogen as dopants in the ZnO crystal lattice (Wang *et al.*, 2015; Nie *et al.*, 2017). Fig. 4(*a*) shows the O *K*-edge of CNZ300, CNZ400, CNZ500 and ZnO. XAS provides important information about O and Zn interactions in ZnO. Electron transitions from 1*s* to 2*p* orbitals in oxygen can be observed in the region between 530 eV and 550 eV. In Fig. 4(*a*), the energy range 530–540 eV represents the interactions between oxygen 2*p* orbitals and Zn 4*s* orbitals. The range 540–550 eV represent the 2*p* interaction in oxygen and 4*p*/4*d* interactions in zinc. In the XAS of the O *K*-edge, the main four absorption features are indicated as A, B, C and D. The transition around 530 eV is due to the hybridization of oxygen 2*p* orbitals to the incomplete 3*d* orbitals of the transition metal. However, in the case of the ZnO O *K*-edge, a shallow shoulder peak merged with peak B can be attributed to very weak interactions between oxygen 2*p* and zinc fully occupied 3*d* orbitals. The main absorption peak B can be observed at 537.34 eV for CNZ500 due to hybridization of 2*p* orbitals of oxygen and 4*s* orbitals of zinc. Absorption peaks C and D are observed in CNZ nanofoams and ZnO. In the case of ZnO, these peaks are comparatively weaker than that of CNZ nanofoams. These absorptions are caused due to the interactions between 2*p* orbitals of oxygen and 4*p* orbitals of zinc. It can be clearly seen in Fig. 4(*a*) that the photon energy peak A (533.3 eV, pure ZnO) is slightly shifted to higher energy (534.04 eV) in CNZ500. This may be caused due to the substitution of oxygen atoms with those of carbon and nitrogen atoms in the crystal lattice (Chiou *et al.*, 2004). A similar shift can be observed for the absorption peak B.

Fig. 4(*b*) shows nitrogen *K*-edge XAS spectra of CNZ300, CNZ400 and CNZ500 confirming nitrogen as a dopant. The spectral features of all CNZ nanofoams are similar with slight differences in the region 403–404 eV. The peaks are named as A, B, C, D (399 eV, 402 eV, 403 eV, 404 eV) and are due to unoccupied 2*p* orbitals of nitrogen and neighbouring ion states. In the ZnO hexagonal crystal structure, when nitrogen replaces oxygen atoms Zn–N bonds are formed. In other words, two kinds of nitrogen metal bonds are possible in CNZ nanofoams: one along the *c* axis called the π bond and the other lying in the (*ab*) plane called the σ bond due to $2p_{xy}$ interactions. So, $2p_{xy}$ and $2p_{zy}$ orbitals interact with 3*d*–4*s* orbitals of Zn and lead to the absorption peaks as A, B, C and D spectral features. Peaks A and B at 399 eV and 402 eV, respectively, are attributed to the Zn–N peak, which arises due to transitions of nitrogen 1*s* electrons to Zn 3*d*–4*s* orbitals. Peaks C and D at 403 eV and 404 eV, respectively, are attributed to nitrogen 1*s* to π^* transitions (Zhong *et al.*, 2012).

Fig. 4(*c*) represents carbon *K*-edge XAS spectra which confirms the presence of carbon in CNZ nanofoams. These peaks arise from unoccupied π^* and σ^* states associated with sp^2 hybridized orbitals of carbon. This proves the presence of carbon as a dopant in the lattice of CNZ nanofoams. Carbon XAS spectra of all the three CNZ nanofoams exhibit four main absorption features in the range 284–291 eV. These absorption features are assigned A, B, C and D (284 eV, 286 eV, 287 eV and 291 eV). A to C indicate the π^* transitions of carbon and D indicates the σ^* transitions. The peak A, at 284 eV, indicates π^* transitions, peak B at 286 eV indicates the π^* C–O transition, peak C at 287 eV indicates the π^* C–O–C/C–N transition and peak D at 291 eV indicates σ^* C–C transitions (Ganguly *et al.*, 2011).

Fig. 4(*d*) shows Zn L_2- and L_3-edge combined XAS spectra of ZnO and CNZ nanofoams. *L*-edge spectra of a 3*d* transition metal are sensitive to interactions with neighbouring atoms as well as the electronic states of the atoms. In Zn *L*-edge XAS spectra, L_3 and L_2 absorption peaks arise due to the electron transition from $2p_{3/2}$ and $2p_{1/2}$ to unoccupied 4*s* and 4*d* levels.

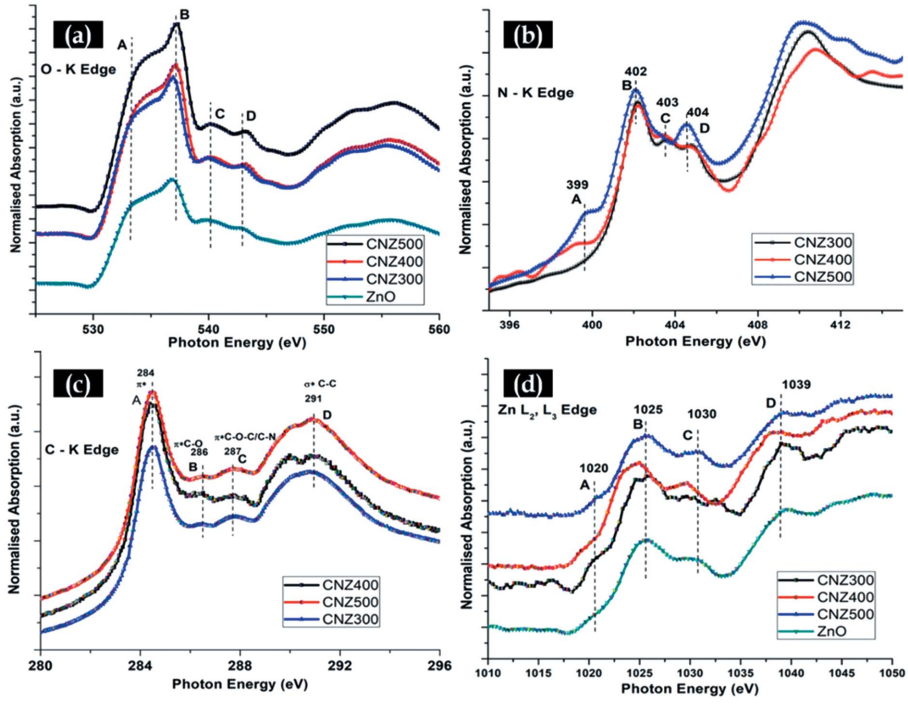

Figure 4
XAS spectroscopy of CNZ300, CNZ400, CNZ500 and ZnO. (*a*) O *K*-edge. (*b*) N *K*-edge. (*c*) C *K*-edge. (*d*) Zn *L*-edge.

The multi-peak structure of the Zn L_3 and L_2 XAS indicates the formation of molecular orbitals, that occur due to strong overlapping or mixing of 3*d* and 4*p* orbitals. Zn L_3-edge absorptions are marked as A, B and C and the L_2-edge absorption peak is marked as D (1020 eV, 1025 eV, 1030 eV and 1039 eV). Peak A is also called a pre-edge peak and appears at a low energy level due to the asymmetry in wurtzite ZnO structure. In other words, the Zn $2p_{3/2}$–4*s* absorption peak represents Peak A at 1020 eV which is similar to the hybridization of 2*p* orbitals of oxygen to 4*s* orbitals of zinc as described in the O *K*-edge XAS. The Zn *L*-edge feature at 1020 eV represents zinc 4*s* transitions while the features above 1025 eV represent zinc 4*d* transitions. Carbon, nitrogen and oxygen when bonded with zinc lead to higher electron intensity due to carbon and nitrogen doping level to Zn 4*d* states. Moreover, O *K*-edge and Zn *L*-edge XAS studies are angle dependent due to the existence of a bilayer σ bond along the *c* axis-oriented π bond. From Fig. 4(*d*) it is clear that the peak intensity increases with an increase in calcination temperature. These changes in the peak intensities are related to the unoccupied density of states. The change in the Zn and O peak intensity clearly indicates the covalent bonds in Zn–O and Zn–C, which leads to an increase in the electron transfer from O 2*p* states, and carbon and nitrogen a doping level to Zn 4*d* states (Byrne *et al.*, 2014). It can be concluded that the absorption intensity increases due to strong overlapping of molecular orbitals with more unoccupied states of neighbouring atoms. Further, the weak pre-edge absorption indicates the distorted crystalline structure that arises due to weak interactions with less electronegative carbon and nitrogen of neighbouring atomic orbitals.

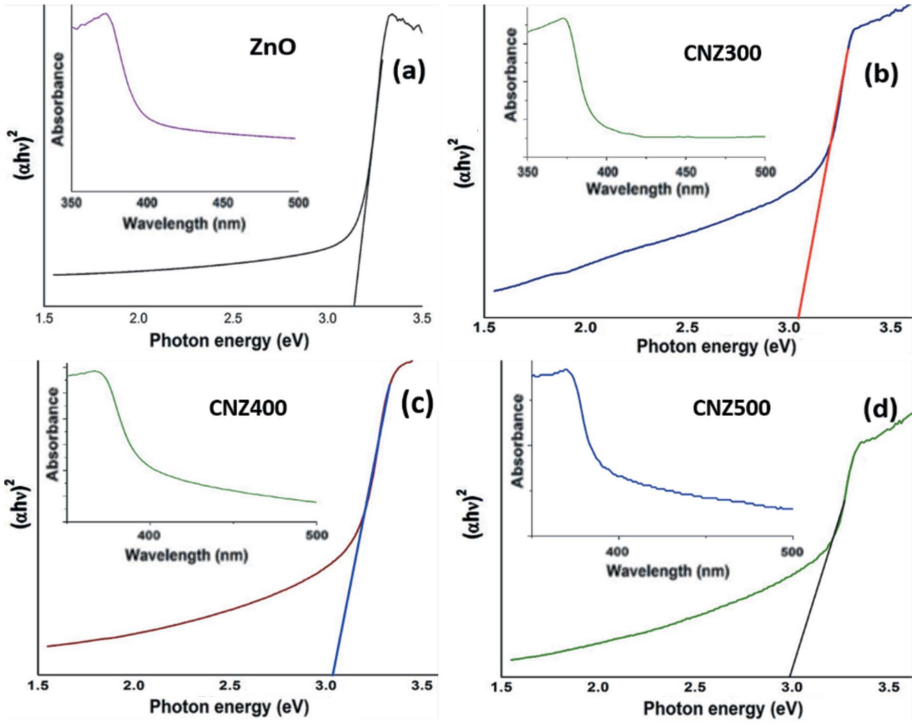

Figure 5
Band gap and UV absorption of (*a*) ZnO, (*b*) CNZ300, (*c*) CNZ400 and (*d*) CNZ500.

3.4. UV–Vis spectroscopy studies

The UV–Vis spectroscopy studies were performed to study the absorption properties of ZnO, CNZ300, CNZ400 and CNZ500. Wurtzite ZnO structure with hexagonal lattice contains Zn^{2+} and O^{2-} ions. Each zinc ion is surrounded by four oxygen ions. This arrangement gives rise to polar symmetry along the hexagonal vertical axis called the *c* axis. The energy differences between the highest occupied molecular orbital (HOMO) and lowest unoccupied molecular orbital (LUMO) formed by the hybridization of Zn *d* orbitals and oxygen 2*p* orbitals causes the band gap, which in turn leads to absorption in the UV–Vis region. Fig. 5 shows absorption spectra of all prepared CNZ nanofoams. The absorption values are observed at 366 nm for ZnO and 369 nm, 372 nm and 373 nm for CNZ300, CNZ400 and CNZ500, respectively. No additional peak is observed except redshift from ZnO to CNZ nanofoams, which indicates that the process of doping did not alter the crystal structure of CNZ nanofoams.

3.5. Band gap of CNZ nanofoams

While ZnO is a direct band gap semiconductor, the band energy (E_g) can be determined using a Tauc plot (Liu *et al.*, 2016). A Tauc plot can be drawn using the UV–Vis absorption results and the following equation,

$$(\alpha h\nu)^2 = C(h\nu - E_g), \tag{5}$$

where α represents the absorption coefficient, h represents Planck's constant, ν is the frequency of light and E_g is the optical band gap. Fig. 5 shows the Tauc graph, which is plotted between $(\alpha h\nu)^2$ and $h\nu$ using the above-mentioned equation, and where extrapolation of the linear part of the graph gives the band gap value. The calculated band gap values are 3.04 eV, 3.04 eV, 2.98 eV and 3.2 eV for CNZ300, CNZ400, CNZ500 and ZnO, respectively. As expected, a difference in the band gap (0.22 eV) has been observed from ZnO to CNZ500. However, the band gap of CNZ500 has decreased when compared with that of CNZ300 and CNZ500 but there is no change in the band gap of CNZ300 and CNZ400.

3.6. Photocatalytic studies

Photocatalytic activity was monitored to investigate the efficiency of CNZ nanofoams under direct sunlight. Fig. 6 shows the UV–Vis absorption results of methylene blue (MB)

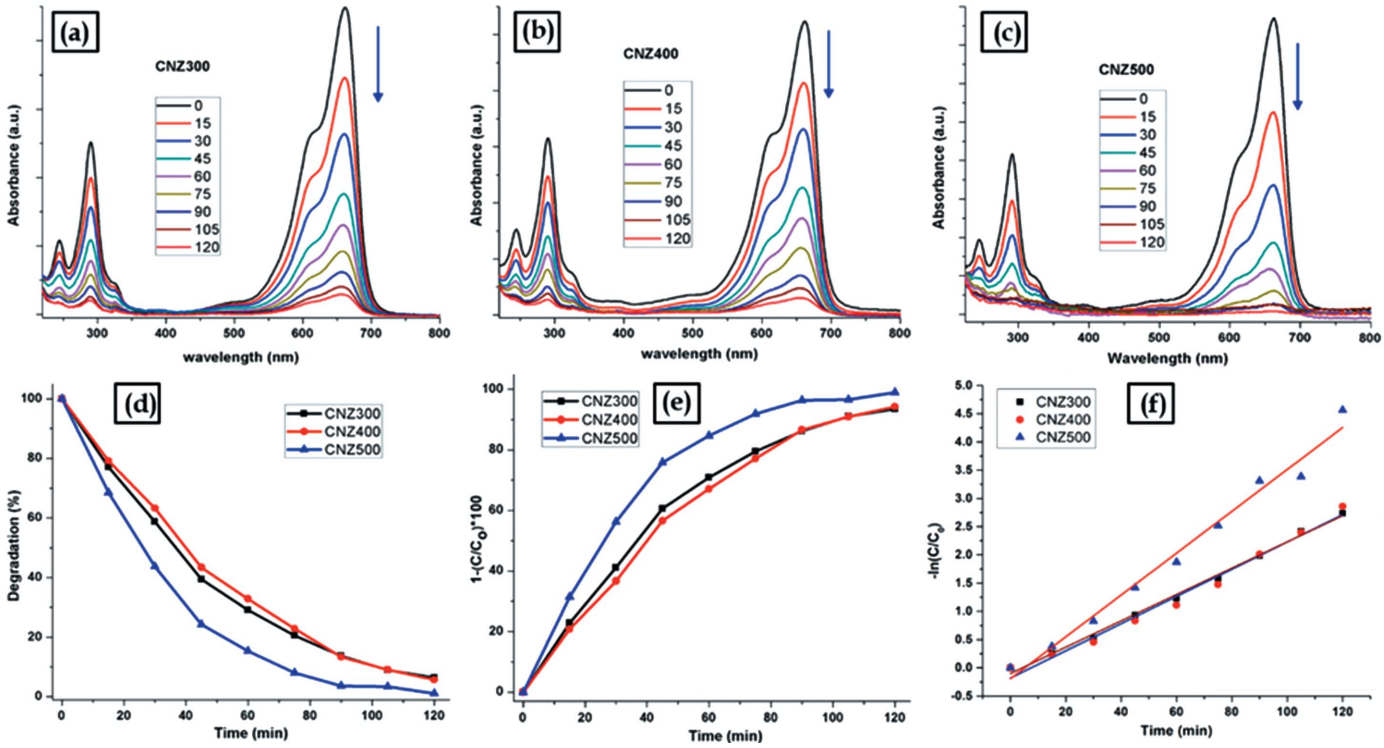

Figure 6
Photocatalytic degradation studies of methylene blue. (*a*) CNZ300, (*b*) CNZ400, (*c*) CNZ500, (*d*)–(*e*) percentage of MB degradation, and (*f*) kinetics.

degradation in the presence of CNZ nanofoams at different time intervals. The absorption spectra clearly show a decrease in the intensity of the absorption peak as a function of irradiation time with no additional peak. This indicates that CNZ nanofoams degrade the MB effectively under direct sunlight irradiation.

Figs. 6(*d*) and 6(*e*) show the degradation percentage calculated for CNZ300, CNZ400 and CNZ500. According to the figure, 76%, 67% and 85%, respectively, of MB has been degraded by CNZ nanofoams in the first 60 min, while the process slowed down to 10%, 19% and 11% for CNZ300, CNZ400 and CNZ500, respectively, for the next 30 min (*i.e.* in the interval 60–90 min). Finally, 7%, 8% and 2% of MB degradation was observed for the last 30 min (*i.e.* in the interval 90–120 min). However, CNZ500 showed 96% degradation within 90 min. Figs. 6(*d*) and 6(*e*) clearly show 93% and 94% of MB degradation using CNZ300 and CNZ400 and 99% of MB degradation using CNZ500 in 120 min. To understand the catalytic efficiency of CNZ nanofoams under sunlight, the degradation results are fitted to a pseudo-first-order reaction kinetics using the following equation,

$$-\ln(C/C_0) = kt, \tag{6}$$

where k represents the rate constant (min^{-1}), C_0 represents the initial concentration and C the concentration of MB at different time intervals. The rate constant k is equal to the slope of the fitting line. All the CNZ nanofoam's photocatalytic MB degradation processes follow Hensel Wood pseudo first-order kinetics with values of k of 0.0233, 0.0240 and 0.037 for CNZ300, CNZ400 and CNZ500, respectively. Thus, the results show that CNZ500 has the highest photodegradation efficacy with 0.037 min^{-1}. Zhang *et al.* (2015) reported a value of 0.0207 min^{-1} for carbon-doped ZnO while Macías-Sánchez *et al.* (2015) reported 0.015 min^{-1} for nitrogen-doped ZnO. We achieved a comparatively higher k value by doping ZnO with carbon and nitrogen.

3.7. Photocatalytic mechanism

Doping is the best method to convert ZnO into visible-light photocatalyst, which leads to the reduction in the band gap by 0.22 eV. After calculating the band gap of ZnO and the prepared CNZ nanofoams, the results clearly show that the band gap has altered from 3.2 eV to 2.9 eV. Doping of carbon and nitrogen atoms to ZnO leads to narrowing of the band gap as they alter the density of states at the valence band. According to molecular orbital theory, 2*p* orbitals of oxygen and 4*s*, 3*d* orbitals of zinc are involved in the formation of molecular orbitals of Zn—O bonds. In CNZ nanofoams, carbon and nitrogen atoms substitute for oxygen atoms in the crystal lattice. These interactions among the 2*p* orbitals of carbon, nitrogen and oxygen with the 4*s* and 3*d* orbitals of zinc lead to the availability of the 2*p* orbitals of carbon and nitrogen above the 2*p* orbitals of oxygen (Miessler *et al.*, 2013). In other words, doping leads to the formation of new energy states above the valence band which causes the narrowing of the band gap of CNZ500 (2.98 eV) as discussed in the UV analysis where it shifts its absorption of light from the UV to the visible range. This shows that the electrons can shift from valence band (VB) to conduction band (CB) by absorbing visible light. Therefore, the CNZ nanofoams can degrade the

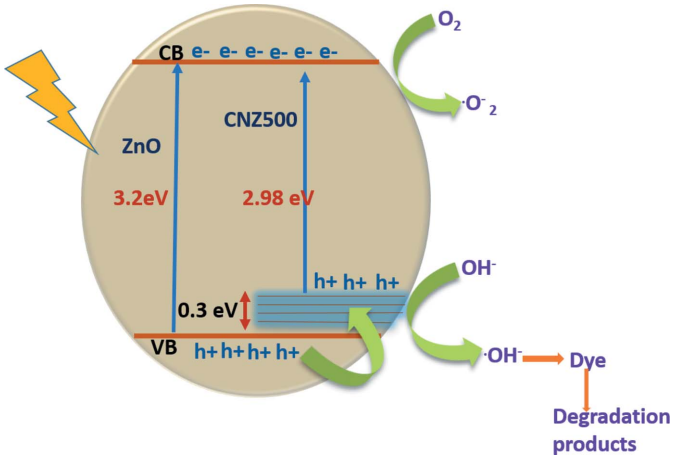

Figure 7
Photocatalytic mechanism for MB degradation of CNZ nanofoams.

dye when irradiated with direct sunlight. Fig. 7 represents the proposed mechanism of the photocatalytic activity of CNZ nanofoams with a reduced band gap. It clearly shows the formation of electron–hole pairs under direct sunlight irradiation. The electrons diffuse into the surface of the catalyst and react with oxygen molecules dissolved in water to yield superoxide radical ions. Simultaneously, the holes that are generated at the valence band diffuse into the surface of the catalyst and lead to the formation of OH radicals from hydroxide ions and H_2O. The hydroxy radical is highly reactive in nature which eventually leads to the degradation of organic pollutants,

$$\text{CNZ nanofoams} + h\nu \rightarrow e^-(\text{CB}) + h^+(\text{VB})$$
$$e^- + O_2 \rightarrow O_2^{-\bullet}$$
$$h^+ + H_2O \rightarrow OH^\bullet + H^+$$
$$O_2^{-\bullet} + H^+ \rightarrow HO_2^\bullet$$
$$OH^\bullet_{ad} + \text{methylene blue} \rightarrow \text{Degradation } (CO_2 + H_2O)$$
$$HO_2^\bullet + \text{methylene blue} \rightarrow \text{Degradation } (CO_2 + H_2O)$$

3.8. Antimicrobial studies

The measured inhibition zone diameter values are listed in Table 2. Fig. S2 of the supporting information shows the zone inhibition antimicrobial activity of loaded CNZ300, CNZ400 and CNZ500 nanofoams. All three CNZ nanofoams exhibit antimicrobial activity against the MDR *E. Fergusonii*. The antimicrobial activity of metal oxide nanoparticles can be affected by many factors such as crystallite size, shape and defects. The results of antimicrobial activity clearly demonstrate that CNZ300 has shown the highest inhibition zone compared with CNZ400 and CNZ500. Calcination in the normal atmosphere may increase the oxygen vacancies on the surface and surface defects. Further, doping in ZnO lattice causes the generation of defects and may increase the generation of reactive oxygen species (ROS) which in turn results in an increase in the antimicrobial activity. As shown in Fig. 8, various mechanisms have been proposed (Azam *et al.*, 2012; Fang *et al.*, 2006; Silvestre *et al.*, 2013; Rago *et al.*, 2014) but the exact mechanism is not clear. Few important paths have been discussed for CNZ nanofoam antimicrobial activity. The cell membrane was damaged by direct contact of CNZ nanofoams. However, the surface properties and defects can affect the antimicrobial activity. Another mechanism is proposed based on Zn ions release. The released Zn^{2+} ions affect the amino acid metabolism, the disruptions in the enzyme action and also the active transport inhibition. Further, many studies considered that ROS generation is a major cause of ZnO antimicrobial activity (Hameed *et al.*, 2016). ROS species such as superoxides, hydroxide radical ions and H_2O_2 are generally produced during the photocatalysis. Releasing these species kills the bacteria by damaging DNA, proteins and lipids (Kiran Kumar *et al.*, 2019).

Table 2
Antimicrobial activity studies of CNZ nanofoams – measured inhibition zone diameter values.

ZnO	1%	5%
CNZ300	12 mm	15 mm
CNZ400	10 mm	13 mm
CNZ500	12 mm	13.5 mm

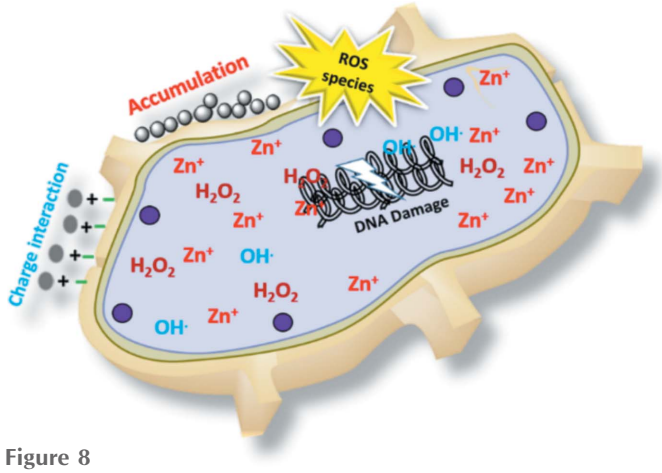

Figure 8
Antimicrobial activity mechanism of CNZ nanofoams.

4. Conclusion

We have successfully synthesized ZnO nanofoams using a soft template for solar photocatalysis in particular for open source water treatment. SEM, XRD and XAS studies were used to study morphology and doping. XAS studies helped to investigate the dopants carbon and nitrogen. As expected, the band gap for CNZ500 reduced to 2.98 eV by incorporating 2*p* levels of both carbon and nitrogen including above the valence band of ZnO. Photocatalytic studies have proven that CNZ nanofoams are potential photocatalysts to degrade MB under solar light with a pseudo-first-order kinetics k value of 0.37 min^{-1} for CNZ500 and degraded MB by almost 100% within 120 min. Finally, these prepared CNZ nanofoams have potentially inhibited the growth of MDR *E. Fergusonii* which

is isolated from wastewater. Therefore, these CNZ nanofoams can be used to remove pathogenic bacteria from wastewater. Hence, it can also be concluded that the reported CNZ nanofoams are efficient photocatalysts to degrade organic pollutions present in industrial effluents.

Acknowledgements

The authors would like to thank to UGC-DAE Indore centre for providing the opportunity to utilize beamline SXAS facilities. Special thanks to Mr Harsimran Singh Bindra for UV analysis. The authors would also like to thank group member Late Vivek Vinjamuri for his assistance in this work.

Funding information

The following funding is acknowledged: UGC-DAE Consortium for Scientific Research.

References

Adoor, S. G., Bhat, S. D., Dionysiou, D. D., Nadagouda, M. N. & Aminabhavi, T. M. (2014). *RSC Adv.* **4**, 52571–52582.
Alexander, L. & Klug, H. P. (1950). *J. Appl. Phys.* **21**, 137–142.
Azam, A., Ahmed, A. S., Oves, M., Khan, M. S., Habib, S. S. & Memic, A. (2012). *Int. J. Nanomed.* **7**, 6003–6009.
Basyooni, M. A., Shaban, M. & El Sayed, A. M. (2017). *Sci. Rep.* **7**, 41716.
Baxter, J. B. & Schmuttenmaer, C. A. (2006). *J. Phys. Chem. B*, **110**, 25229–25239.
Bindu, P. & Thomas, S. (2014). *J. Theor. Appl. Phys.* **8**, 123–134.
Byrne, J. M., Coker, V. S., Cespedes, E., Wincott, P. L., Vaughan, D. J., Pattrick, R. A. D., van der Laan, G., Arenholz, E., Tuna, F., Bencsik, M., Lloyd, J. R. & Telling, N. D. (2014). *Adv. Funct. Mater.* **24**, 2518–2529.
Chiou, J. W., Jan, J. C., Tsai, H. M., Bao, C. W., Pong, W. F., Tsai, M., Hong, I., Klauser, R., Lee, J. F., Wu, J. J. & Liu, S. C. (2004). *Appl. Phys. Lett.* **84**, 3462–3464.
Cho, J., Lin, Q., Yang, S., Simmons, J. G., Cheng, Y., Lin, E., Yang, J., Foreman, J. V., Everitt, H. O., Yang, W., Kim, J. & Liu, J. (2012). *Nano Res.* **5**, 20–26.
Das, S., Sinha, S., Das, B., Jayabalan, R., Suar, M., Mishra, A., Tamhankar, A. J., Stålsby Lundborg, C. & Tripathy, S. K. (2017). *Sci. Rep.* **7**, 104.
Dharupaneedi, S. P., Anjanapura, R. V., Han, J. M. & Aminabhavi, T. M. (2014). *Ind. Eng. Chem. Res.* **53**, 14474–14484.
Du, Y. K., Yang, P., Mou, Z. G., Hua, N. P. & Jiang, L. (2006). *J. Appl. Polym. Sci.* **99**, 23–26.
Dutta, R. K., Nenavathu, B. P. & Talukdar, S. (2014). *Colloids Surf. B Biointerfaces*, **114**, 218–224.
Dvorak, M., Wei, S. H. & Wu, Z. (2013). *Phys. Rev. Lett.* **110**, 016402.
Fang, M., Chen, J. H., Xu, X. L., Yang, P. H. & Hildebrand, H. F. (2006). *Int. J. Antimicrob. Agents*, **27**, 513–517.
Fiorentino, A., Ferro, G., Alferez, M. C., Polo-López, M. I., Fernández-*Iba*ñez, P. & Rizzo, L. (2015). *J. Photochem. Photobiol. B*, **148**, 43–50.
Game, O., Singh, U., Gupta, A. A., Suryawanshi, A., Banpurkar, A. & Ogale, S. (2012). *J. Mater. Chem.* **22**, 17302.
Ganguly, A., Sharma, S., Papakonstantinou, P. & Hamilton, J. (2011). *J. Phys. Chem. C*, **115**, 17009–17019.
Ghosh, S., Sanjeev, B., Gupta, M. & Kiran Kumar, A. B. V. (2018). *Ceram. Int.* **43**, 1314–1321.
Gupta, A., Saurav, J. R. & Bhattacharya, S. (2015). *RSC Adv.* **5**, 71472–71481.
Haibo, O., Feng, H. J., Cuiyan, L., Liyun, C. & Jie, F. (2013). *Mater. Lett.* **111**, 217–220.
Hameed, A. S. H., Karthikeyan, C., Ahamed, A. P., Thajuddin, N., Alharbi, N. S., Alharbi, S. A. & Ravi, G. (2016). *Sci. Rep.* **6**, 24312.
Huang, C., Shi, R., Amini, A., Wu, Z., Xu, S., Zhang, L., Cao, W., Feng, J., Song, H., Shi, Y., Wang, N. & Cheng, C. (2015). *Sci. Rep.* **5**, 8226.
Kadiyala, U., Tulari-Emre, E. S., Bahng, J. H., Kotov, N. A. & VanEpps, J. S. (2018). *Nanoscale*, **10**, 4927–4939.
Khan, A., Ahmed, M. I., Adam, A., Azad, A. M. & Qamar, M. (2017). *Nanotechnology*, **28**, 055602.
Khoa, N. T., Kim, S. W., Van Thuan, D., Yoo, D., Kim, E. J. & Hahn, S. H. (2014). *CrystEngComm*, **16**, 1344–1350.
Kiran Kumar, A. B. V. & Sanjeev, B. (2018). *Ecofriendly and facile Synthesis of Carbon and Nitrogen Co-doped Zinc Oxide Nanofoams (CNZnO nanofoams)*. Indian patent publication number 34/2019, published date 23 August 2019.
Kiran Kumar, A. B. V., Saila, E. S., Narang, P., Aishwarya, M., Raina, R., Gautam, M. & Shankar, E. G. (2019). *Inorg. Chem. Commun.* **100**, 101–106.
Krishna Rao, K. S. V., Vijaya Kumar Naidu, B., Subha, M. C. S., Sairam, M., Mallikarjuna, N. N. & Aminabahvi, T. M. (2006). *Carbohydr. Polym.* **66**, 345–351.
Kumar, A., Billa, S., Chaudhary, S., Kiran Kumar, A. B. V., Ramana, Ch. V. V. & Kim, D. (2018). *Inorg. Chem. Commun.* **97**, 191–195.
Kumar, S. G. & Rao, K. S. R. K. (2017). *Appl. Surf. Sci.* **391**, 124–148.
Liu, H., Raza, A., Aili, A., Lu, J., AlGhaferi, A. & Zhang, T. (2016). *Sci. Rep.* **6**, 25414.
Macías-Sánchez, J. J., Hinojosa-Reyes, L., Caballero-Quintero, A., de la Cruz, W., Ruiz-Ruiz, E., Hernández-Ramírez, A. & Guzmán-Mar, J. L. (2015). *Photochem. Photobiol. Sci.* **14**, 536–542.
Magalad, V. T., Gokavi, G. S., Raju, K. V. S. N. & Aminabhavi, T. M. (2010). *J. Membr. Sci.* **354**, 150–161.
Miessler, G. L., Fischer, P. J. & Tarr, D. A. (2013). Editors. *Inorganic Chemistry*, 5th ed., p. 134. Pearson.
Nie, Y., Wang, Z., Wang, J., Bao, F., Zhang, J., Ma, Y., Sham, T. & Sun, X. (2017). *J. Phys. Chem. C*, **121**, 26076–26085.
Pascariu, P., Tudose, I. V., Suchea, M., Koudoumas, E., Fifere, N. & Airinei, A. (2018). *Appl. Surf. Sci.* **448**, 481–488.
Pasupuleti, C., Bhagat, N., Vermani, M. & Singh, S. (2017). *Escherichia fergusonii strain MNCS1 16S ribosomal RNA gene*, partial sequence. doi: 10.13140/RG.2.2.23443.58403.
Qi, K., Cheng, B., Yu, J. & Ho, W. (2017). *J. Alloys Compd.* **727**, 792–820.
Rago, I., Chandraiahgari, C. R., Bracciale, M. P., De Bellis, G., Zanni, E., Cestelli Guidi, M., Sali, D., Broggi, A., Palleschi, C., Sarto, M. S. & Uccelletti, D. (2014). *RSC Adv.* **4**, 56031–56040.
Rani, B., Punniyakoti, S. & Sahu, N. K. (2018). *New J. Chem.* **42**, 943–954.
Rao, J., Yu, A., Shao, C. & Zhou, X. (2012). *Appl. Mater. Interfaces*, **4**, 5346–5352.
Reddy, K. M., Sairam, M., Babu, V. R., Subha, M. C. S., Chowdojirao, K. & Aminabhavi, T. M. (2007). *Des. Monomers Polym.* **10**, 297–309.
Ruqia, B., Nam, K. M., Lee, H., Lee, G. & Choi, S. (2017). *CrystEngComm*, **19**, 1454–1458.
Show, B., Mukherjee, N. & Mondal, A. (2016). *RSC Adv.* **6**, 75347–75358.
Silva, G. T. S. T. da, Carvalho, K. T. G., Lopes, O. F., Gomes, E. S., Malagutti, A. R., Mastelaro, V. R., Ribeiro, C. & Mourão, H. A. J. L. (2017). *ChemCatChem*, **9**, 3795–3804.
Silvestre, C., Cimmino, S., Pezzuto, M., Marra, A., Ambrogi, V., Dexpert-Ghys, J., Verelst, M., Augier, S., Romano, I. & Duraccio, D. (2013). *Polym. J.* **45**, 938–945.
Wang, M., Ren, F., Zhou, J., Cai, G., Cai, L., Hu, Y., Wang, D., Liu, Y., Guo, L. & Shen, S. (2015). *Sci. Rep.* **5**, 12925.
Wang, S., Kuang, P., Cheng, B., Yu, J. & Jiang, C. (2018). *J. Alloys Compd.* **741**, 622–632.
Wang, Y. & Cui, Z. (2009). *J. Phys. Conf. Ser.* **152**, 012021.

Yu, W., Zhang, J. & Peng, T. (2016). *Appl. Catal. Environ.* **181**, 220–227.
Zhang, X., Qin, J., Hao, R., Wang, L., Shen, X., Yu, R., Limpanart, S., Ma, M. & Liu, R. (2015). *J. Phys. Chem. C*, **119**, 20544–20554.
Zhang, Y.-Z., Wu, L.-H., Liu, Y.-P., Xie, E.-Q., Yan, D. & Chen, J.-T. (2009). *Chin. Phys. Lett.* **26**, 038201.
Zhong, J., Deng, J., Mao, B., Xie, T., Sun, X., Mou, Z., Hong, C., Yang, P. & Wang, S. (2012). *Carbon*, **50**, 335–338.